

## Structures of Metallosupramolecular Coordination Assemblies Can Be Obtained by Ion Mobility Spectrometry–Mass Spectrometry

Erin R. Brocker,<sup>†</sup> Stanley E. Anderson,<sup>†,‡</sup> Brian H. Northrop,<sup>§</sup> Peter J. Stang,<sup>||</sup> and Michael T. Bowers<sup>\*,†</sup>

*Department of Chemistry & Biochemistry, University of California, Santa Barbara, California 93106, Department of Chemistry, Westmont College, Santa Barbara, California 93108, Department of Chemistry, Wesleyan University, Middletown, Connecticut 06459, and Department of Chemistry, University of Utah, 315 South 1400 East, Room 2020, Salt Lake City, Utah 84112*

Received June 29, 2010; E-mail: bowers@chem.ucsb.edu

**Abstract:** Rigid rectangular, triangular, and prismatic supramolecular assemblies, cyclobis[(2,9-bis[*trans*-Pt(PEt<sub>3</sub>)<sub>2</sub>(PF<sub>6</sub>)]anthracene)(4,4'-dipyridyl)], cyclotris[(2,9-bis[*trans*-Pt(PEt<sub>3</sub>)<sub>2</sub>(PF<sub>6</sub>)]phenanthrene)(4,4'-dipyridyl)], and cyclotris[bis[*cis*-Pt(PEt<sub>3</sub>)<sub>2</sub>(CF<sub>3</sub>SO<sub>3</sub>)<sub>2</sub>]tetrakis(4-pyridyl)cyclobutadienecyclopentadienylcobalt(I)], respectively, based on dipyridyl ligands and square planar platinum coordination, have been investigated by ion mobility spectrometry–mass spectrometry (IMS-MS). Electrospray ionization–quadrupole and time-of-flight spectra have been obtained and fragmentation pathways assigned. Ion mobility studies give cross sections that compare very well with cross sections of the supramolecular rectangle and triangle species on the basis of X-ray bond distances. For the larger prism structures, agreement of experimental and calculated cross sections from molecular modeling is very good, indicating IMS-MS methods can be used to characterize complex self-assembled structures where X-ray or other spectroscopic structures are not available.

### Introduction

Coordination-driven self-assembly is a technique that has been increasingly used in nanofabrication to generate supramolecular nanomaterials for a number of applications. Supramolecular assemblies have been used in crystal engineering to create optical<sup>1</sup> and electronic devices.<sup>2</sup> Molecular recognition systems have employed supramolecular coordination assemblies in host–guest complexes,<sup>3–7</sup> as molecular switches,<sup>8–10</sup> and in catalysis.<sup>11,12</sup> Coordination-driven self-assembly is a bottom-up technique, and as such it must be highly convergent to

produce defect-free materials at any synthesis scale. Unambiguous characterization of these supramolecular assemblies is critical to understanding whether the synthesis is successful or not and to understanding their performance, given that the desired assembly may not be accessible via an absolute route.<sup>13</sup>

Various mass spectrometry (MS) techniques have been previously used to elucidate the structures, fragmentation pathways, and thermodynamic properties of supramolecular complexes.<sup>14–17</sup> Ion mobility spectrometry–mass spectrometry (IMS-MS) provides a method to characterize the shape of supramolecular assemblies that cannot be unambiguously characterized through traditional methods such as X-ray crystallography or NMR due to obstacles such as insolubility or symmetry between isomers. Recently, traveling wave ion mobility mass spectrometry was successfully used to obtain qualitative conformational information and high-resolution mass

<sup>†</sup> University of California, Santa Barbara.

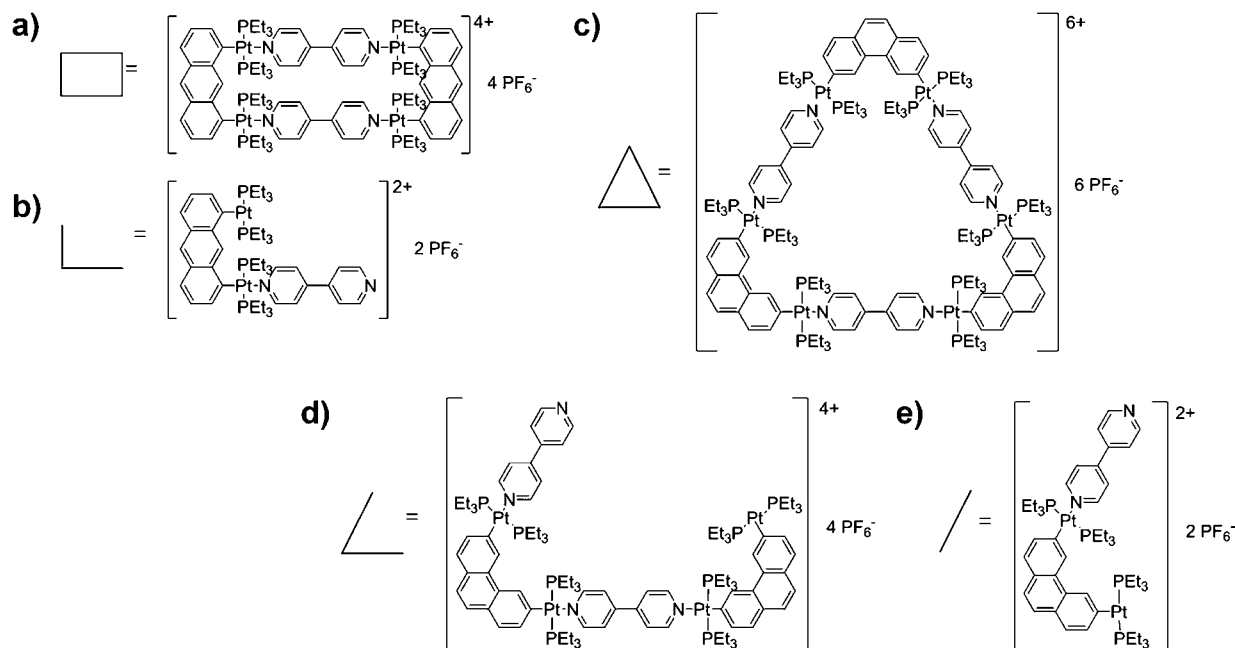
<sup>‡</sup> Westmont College.

<sup>§</sup> Wesleyan University.

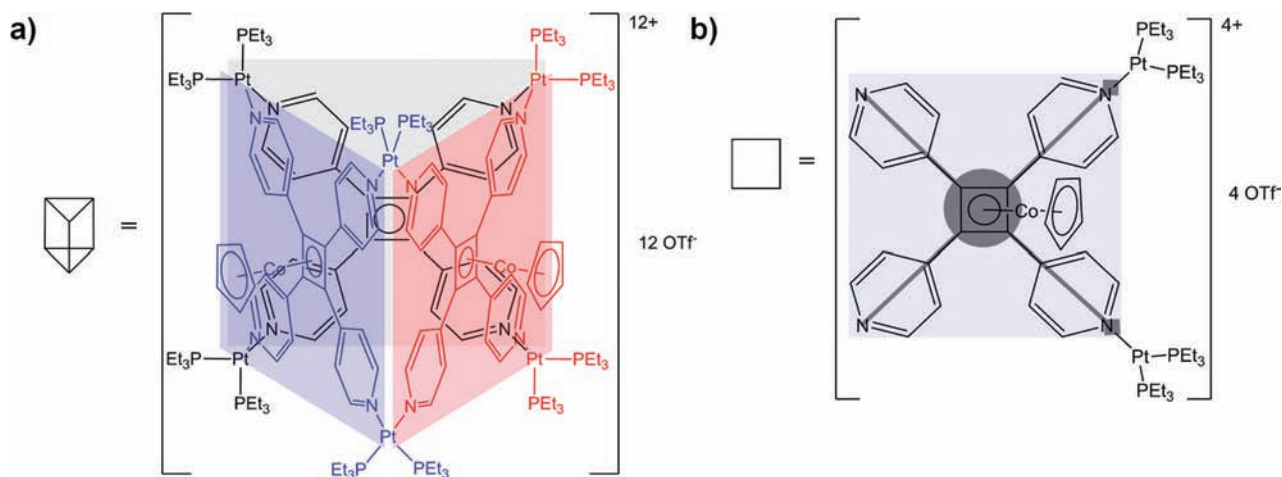
<sup>||</sup> University of Utah.

- (1) de Silva, A. P.; McCaughan, B.; McKinney, B. O. F.; Querol, M. *Dalton Trans.* **2003**, 1902–1913.
- (2) Sun, L.-P.; Niu, S.-Y.; Jin, J.; Yang, G.-D.; Ye, L. *Inorg. Chem. Commun.* **2006**, *9*, 679–682.
- (3) Seidel, S. R.; Stang, P. J. *Acc. Chem. Res.* **2002**, *35*, 972–983.
- (4) Raymond, K. N.; Andersen, U. N.; Seeber, G.; Fiedler, D.; Lin, D.; Harris, D. *J. Am. Soc. Mass. Spectrom.* **2006**, *17*, 292–296.
- (5) Tashiro, S.; Tominaga, M.; Yamaguchi, Y.; Kato, K.; Fujita, M. *Angew. Chem., Int. Ed.* **2006**, *45*, 241–244.
- (6) Tashiro, S.; Tominaga, M.; Yamaguchi, Y.; Kato, K.; Fujita, M. *Chem.—Eur. J.* **2006**, *12*, 3211–3217.
- (7) Pluth, M. D.; Fiedler, D.; Mugridge, J. S.; Bergman, R. G.; Raymond, K. N. *Proc. Natl. Acad. Sci. U.S.A.* **2009**, *106*, 10438–10443.
- (8) Lusby, P. J.; Müller, P.; Pike, S. J.; Slawin, A. M. Z. *J. Am. Chem. Soc.* **2009**, *131*, 16398–16400.
- (9) Jimenez-Molero, M. C.; Dietrich-Buchecker, C.; Sauvage, J. P. *Chem.—Eur. J.* **2002**, *8*, 1456–1466.
- (10) Bonnet, S.; Collin, J. P.; Koizumi, M.; Mobian, P.; Sauvage, J. P. *Adv. Mater.* **2006**, *18*, 1239–1250.

- (11) Gianneschi, N. C.; Bertin, P. A.; Nguyen, S. T.; Mirkin, C. A.; Zakharov, L. N.; Rheingold, A. L. *J. Am. Chem. Soc.* **2003**, *125*, 10508–10509.
- (12) Masar, M. S.; Gianneschi, N. C.; Oliveri, C. G.; Stern, C. L.; Nguyen, S. T.; Mirkin, C. A. *J. Am. Chem. Soc.* **2007**, *129*, 10149–10158.
- (13) Northrop, B. H.; Zheng, Y.-R.; Chi, K.-W.; Stang, P. J. *Acc. Chem. Res.* **2009**, *42*, 1554–1563.
- (14) Zhao, L.; Ghosh, K.; Zheng, Y.; Lyndon, M. M.; Williams, T. I.; Stang, P. J. *Inorg. Chem.* **2009**, *48*, 5590–5592.
- (15) Schalley, C. A.; Müller, T.; Linnartz, P.; Witt, M.; Schäfer, M.; Lützen, A. *Chem.—Eur. J.* **2002**, *8*, 3538–3551.
- (16) Hopfgartner, G.; Piguet, C.; Henion, J. D. *J. Am. Soc. Mass. Spectrom.* **1994**, *5*, 748–756.
- (17) Baytekin, B.; Baytekin, H. T.; Schalley, C. A. *Org. Biomol. Chem.* **2006**, *4*, 2825–2841.



**Figure 1.** Structures of (a) fully assembled  $\text{Rect}(\text{PF}_6)_4$  and (b) its monomer fragment  $\text{Rect}_{1/2}(\text{PF}_6)_2$  and of (c) fully assembled  $\text{Tri}(\text{PF}_6)_6$ , (d) its dimer fragment  $\text{Tri}_{2/3}(\text{PF}_6)_4$ , and (e) its monomer fragment  $\text{Tri}_{1/3}(\text{PF}_6)_2$ .



**Figure 2.** Postulated structures of (a) the fully assembled  $\text{Prism}(\text{OTf})_{12}$  and (b) its monomer  $\text{Prism}_{1/3}(\text{OTf})_4$ . In (a) the rear Cp-Co group is omitted for clarity, and in (b) square boxes at the tip of the diagonal lines represent  $\text{Pt}^{2+}$  centers.

spectra of hexacadmium macrocycles.<sup>18</sup> Here we use drift cell IMS-MS to obtain absolute cross sections of a number of coordination-driven supramolecular assemblies. These cross sections can be compared to those obtained from X-ray structures of simple square and triangular species, and they can be compared with state-of-the-art molecular modeling for a more complex prismatic assembly for which X-ray structures are not available. This latter application allows unambiguous structural confirmation even when traditional X-ray and spectroscopic methods fail.

## Experimental Section

**Compounds.** Syntheses of the supramolecular rectangle<sup>19</sup> and triangle<sup>20</sup> have been reported previously, and their structures are shown in Figure 1. The structure of the prism<sup>21</sup> has been postulated (Figure 2) and is consistent with NMR studies, but it was not possible to obtain crystals for a definitive X-ray structure. For our

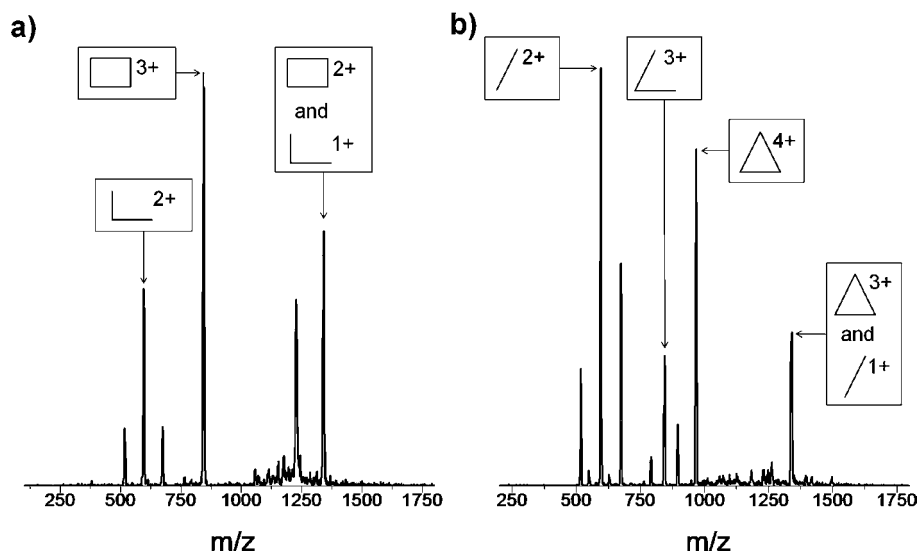
ion mobility work, the hexafluorophosphate salts of the rectangle, cyclobis[(2,9-bis[*trans*-Pt( $\text{PEt}_3$ )<sub>2</sub>( $\text{PF}_6$ )]anthracene)(4,4'-dipyridyl)], and the triangle, cyclotris[(2,9-bis[*trans*-Pt( $\text{PEt}_3$ )<sub>2</sub>( $\text{PF}_6$ )]phenanthrene)(4,4'-dipyridyl)], and the triflate salt of the prism, cyclotris[bis[*cis*-Pt( $\text{PEt}_3$ )<sub>2</sub>( $\text{CF}_3\text{SO}_3$ )<sub>2</sub>](tetrakis(4-pyridyl)cyclobutadienecyclopentadienylcobalt(I))], were used. For simplicity, these salts are abbreviated as  $\text{Rect}(\text{PF}_6)_4$ ,  $\text{Tri}(\text{PF}_6)_6$ , and  $\text{Prism}(\text{OTf})_{12}$ . Loss of  $\text{PF}_6^-$  or  $\text{OTf}^-$  from these salts occurs during electrospray ionization to yield positive ions with a total charge equal to the number of removed counterions. An example of a charged species is  $[\text{Tri}(\text{PF}_6)_2]^{4+}$ , where four  $\text{PF}_6^-$  counterions have been lost.

**Ion Mobility Spectrometry–Mass Spectrometry.** The IMS-MS instrument used for these experiments has been described previously,<sup>22</sup> but a short description of the experimental procedure is provided here. Stock solutions of the analyte are diluted to 10

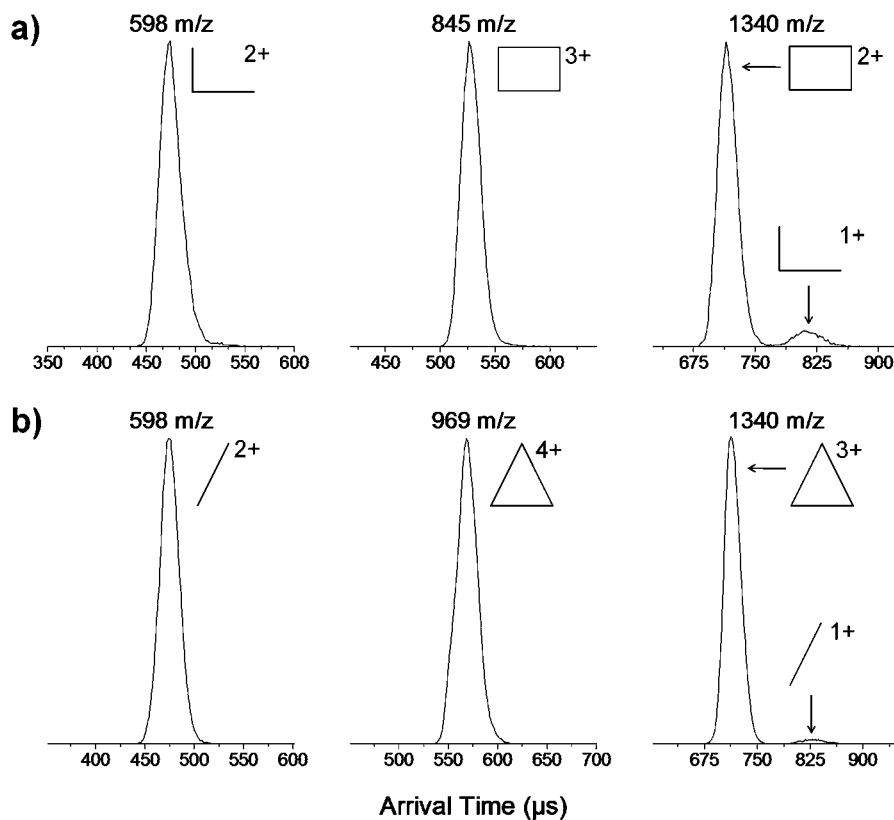
(18) Chan, Y.-T.; Li, X.; Soler, M.; Wang, J.-L.; Wesdemiotis, C.; Newkome, G. R. *J. Am. Chem. Soc.* **2009**, *131*, 16395–16397.

(19) Kuehl, C. J.; Mayne, C. L.; Arif, A. M.; Stang, P. J. *Org. Lett.* **2000**, *2*, 3727–3729.

(20) Kryshchenko, Y. K.; Seidel, S. R.; Arif, A. M.; Stang, P. J. *J. Am. Chem. Soc.* **2003**, *125*, 5193–5198.



**Figure 3.** ESI-quadrupole mass spectra of Rect(PF<sub>6</sub>)<sub>4</sub> and Tri(PF<sub>6</sub>)<sub>6</sub> with peaks of interest assigned. For the structures representing each symbol, see Figure 1.



**Figure 4.** Arrival time distributions for the  $m/z$  corresponding to (a) the 2+, 3+, and 4+ charge states of the rectangle and (b) the 3+, 4+, and 6+ charge states of the triangle.

$\mu\text{M}$  in reagent-grade acetone just prior to analysis by IMS-MS. The sample is ionized by electrospray using a hollow, gold-coated glass needle loaded with a small amount of analyte solution. After passing through a capillary, the ions enter an ion funnel which focuses the beam, desolvates the ions, and traps them. Ion packets are then pulsed into the drift cell at low energy and are thermalized by collisions with He gas (about 5 Torr). The ions drift through

the cell under the influence of a weak electric field, exit, and are mass-selected and detected as a function of time, generating an arrival time distribution (ATD).






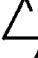



The arrival time  $t_A$  can be related to the reduced mobility  $K_0$  via eq 1,<sup>23</sup>

$$t_A = \frac{l^2}{K_0} \frac{1}{760} \frac{273}{T} \left( \frac{p}{V} \right) + t_0 \quad (1)$$

where  $l$  is the cell length,  $T$  the temperature,  $p$  the pressure,  $V$  the voltage across the cell, and  $t_0$  the time spent after exiting the cell until reaching the detector. Plotting the arrival time ( $t_A$ ) vs  $p/V$  gives

- (21) Caskey, D. C.; Yamamoto, T.; Addicott, C.; Shoemaker, R. K.; Vacek, J.; Hawkrige, A. M.; Muddiman, D. C.; Kottas, G. S.; Michl, J.; Stang, P. J. *J. Am. Chem. Soc.* **2008**, *130*, 7620–7628.  
 (22) Wytenbach, T.; Kemper, P. R.; Bowers, M. T. *Int. J. Mass Spectrom.* **2001**, *212*, 13–23.

**Table 1.** Experimental and X-ray Cross Sections for the Rectangle and Triangle Species

Ion	m/z	$\sigma_{\text{expt}}$ ( $\text{\AA}^2$ )	$\sigma_{\text{calc}}^{\text{sig. } a}$ ( $\text{\AA}^2$ )	$\sigma_{\text{calc}}^{\text{trj. } b}$ ( $\text{\AA}^2$ )
[Rect(PF <sub>6</sub> ) <sub>2</sub> ] <sup>2+</sup> 	1340	362	357	371
[Rect(PF <sub>6</sub> )] <sup>3+</sup> 	845	361	357	373
[Rect <sub>1/2</sub> ] <sup>2+</sup> 	598	223	226	233
[Rect <sub>1/2</sub> (PF <sub>6</sub> )] <sup>1+</sup> 	1340	227	226	226
[Tri(PF <sub>6</sub> ) <sub>3</sub> ] <sup>3+</sup> 	1340	577	571	582
[Tri(PF <sub>6</sub> ) <sub>2</sub> ] <sup>4+</sup> 	969	642 <sup>c</sup>	642	681
[Tri(PF <sub>6</sub> ) <sub>2</sub> ] <sup>4+</sup> 	969	580	568	583
[Tri <sub>1/3</sub> (PF <sub>6</sub> )] <sup>1+</sup> 	1340	242	251	249
[Tri <sub>1/3</sub> ] <sup>2+</sup> 	598	243	243	251

<sup>a</sup> sig = projection approximation;<sup>35,36</sup> the bond distances were taken from the X-ray structures in refs 19 and 20. <sup>b</sup> trj = trajectory method;<sup>37</sup> the bond distances were taken from the X-ray structures of refs 19 and 20. <sup>c</sup> Open Tri<sup>4+</sup> ion observed at 77 K; cross section is an estimate.

a straight line with intercept  $t_0$  and a slope proportional to  $1/K_0$ . The cross section  $\sigma$  is then calculated (eq 2) from  $K_0$  using kinetic theory,<sup>24</sup> where  $q$  is the ion charge,  $N$  the gas density in the cell,  $\mu$  the ion–He reduced mass, and  $k_B$  the Boltzmann constant.

$$\sigma = \frac{3q}{16NK_0} \left( \frac{2\pi}{\mu k_B T} \right)^{1/2} \quad (2)$$

High-resolution mass spectra were obtained on a prototype of the commercially available Synapt HDMS instrument (Waters, Manchester, U.K.), which features a high-resolution quadrupole time-of-flight (Q-TOF) mass spectrometer similar to the commercial Q-TOF 2 instrument (Waters, Manchester, U.K.).

**Computational Modeling.** Molecular modeling of these systems was carried out using the Discovery 3 protocol of the Insight 2005 package of programs produced by Accelrys<sup>25</sup> since the ESFF force field<sup>26</sup> is parametrized to incorporate transition metals in a variety of coordination geometries. We validated the calculations by testing this program package against our AMBER modeling of a series of polyhedral oligomeric silsesquioxanes (POSS) oligomers previously studied<sup>27</sup> and reproduced the cross sections exactly for a nearly identical distribution of structures. In the current study, the PDB coordinates from X-ray structures of Rect(PF<sub>6</sub>)<sub>4</sub> and Tri(PF<sub>6</sub>)<sub>6</sub> were input into Insight, the ESFF force field was assigned and updated using the X-ray bond distances, and simulated annealing was carried out to obtain low-energy structures. Our annealing protocol utilizes repeated cycles of high-temperature heating, cooling, and energy minimization. This annealing protocol typically heats structures to

1400 K for 5–10 ps and then cools exponentially for 30 ps to 50 K before energy minimization. Anions are handled using a built-in distance restraint so that they do not “dissociate” at high temperature. At least 50–100 candidate structures are employed to generate a diagnostic graph of calculated cross sections versus relative energy.<sup>27,28</sup>

## Results and Discussion

**Rectangle and Triangle IMS-MS.** Rect(PF<sub>6</sub>)<sub>4</sub> and Tri(PF<sub>6</sub>)<sub>6</sub> are self-assembled via the same coordination-driven reaction, though they utilize different isomeric linkages of bis-Pt(II) ligands where the available Pt coordination sites are oriented 90° and 60° relative to each other, respectively, to produce the two structures. Rect(PF<sub>6</sub>)<sub>4</sub> and Tri(PF<sub>6</sub>)<sub>6</sub> may be considered cyclic dimers and trimers of the monomers shown in Figure 1b,e. The monomer fragment of the rectangle is abbreviated as Rect<sub>1/2</sub>(PF<sub>6</sub>)<sub>2</sub>, and the monomer and dimer fragments of the triangle are abbreviated as Tri<sub>1/3</sub>(PF<sub>6</sub>)<sub>2</sub> and Tri<sub>2/3</sub>(PF<sub>6</sub>)<sub>4</sub>.

As mentioned previously, the coordination complexes are ionized by removal of one or more PF<sub>6</sub><sup>−</sup> counterions. While our primary interest here is in structural characterization of the fully assembled supramolecular complexes, it is possible for lower charge-state fragments of the rectangle and triangle to appear at the same  $m/z$  as the parent ion. Hence, these species also need to be structurally characterized if they are present. For example, [Tri<sub>1/3</sub>(PF<sub>6</sub>)]<sup>+</sup>, [Tri<sub>2/3</sub>(PF<sub>6</sub>)<sub>2</sub>]<sup>2+</sup>, and [Tri(PF<sub>6</sub>)<sub>3</sub>]<sup>3+</sup> could all appear at  $m/z$  598. However, some charge states of the coordination complexes are unique to the fully assembled complexes only. Examples are [Rect(PF<sub>6</sub>)<sub>3</sub>]<sup>3+</sup> ( $m/z$  845) and [Tri(PF<sub>6</sub>)<sub>2</sub>]<sup>4+</sup> ( $m/z$  969). It is not possible to have any other structures corresponding to these  $m/z$  values since a fraction of

(23) Gidden, J.; Baker, E. S.; Ferzoco, A.; Bowers, M. T. *Int. J. Mass Spectrom.* **2005**, *240*, 183–193.

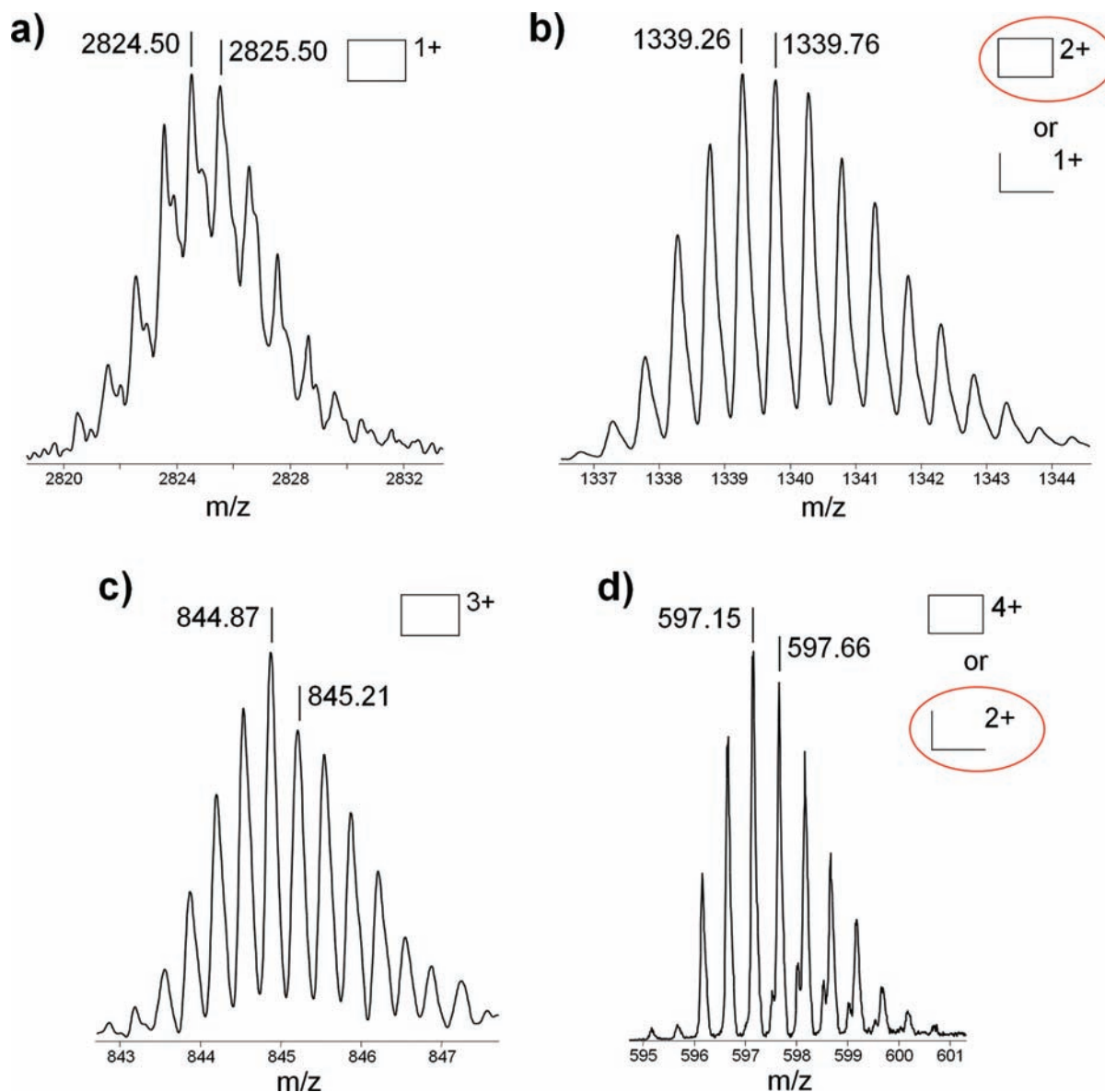
(24) McDaniel, E. W.; Mason, E. A. *The Mobility and Diffusion of Ions in Gases*; Wiley: New York, 1973.

(25) *Insight II*; Accelrys: San Diego, CA, 2005.

(26) Shi, S.; Yan, L.; Yang, Y.; Fisher-Shaulsky, J.; Thacher, T. J. *Comput. Chem.* **2003**, *24*, 1059–1076.

(27) Anderson, S. E.; Baker, E. S.; Mitchell, C.; Haddad, T. S.; Bowers, M. T. *Chem. Mater.* **2005**, *17*, 2537–2545.

(28) Anderson, S. E.; Mitchell, C.; Haddad, T. S.; Vij, A.; Schwab, J. J.; Bowers, M. T. *Chem. Mater.* **2006**, *18*, 1490–1497.



**Figure 5.** Rectangle isotopic distributions for high-resolution mass spectrum peaks (a) 2824  $m/z$  with 1.0 amu spacing, (b) 1340  $m/z$  with 0.5 amu spacing, (c) 845  $m/z$  with 0.33 amu spacing, and (d) 598  $m/z$  with 0.5 amu spacing. The circled structure is the actual species present. See Figure 1 caption for symbol definitions. See Figure S1 in the Supporting Information for comparison with simulated isotopic distributions.

the counterion would be required (e.g.,  $[\text{Rect}_{1/2}(\text{PF}_6)_{1/2}]^{1.5+}$  ( $m/z$  845) is not a reasonable species).

Electrospray ionization (ESI)–quadrupole mass spectra for both the rectangle and triangle are shown in Figure 3. These mass spectra also include peaks in addition to those expected for the fully assembled rectangle and triangle, indicating incomplete assembly, degradation of the sample by loss of bipyridine ligands, a change in charge state of the metals during ESI, or some combination thereof. Acetone solutions of the compounds stored on the benchtop for a few hours exhibited increased degradation in both the mass spectra and ATDs.

An example of the assignment of the various structures depicted in Figure 3 follows. We know from examination of the coordination complexes that the charged species  $[\text{Rect}(\text{PF}_6)]^{3+}$  ( $m/z$  845) and  $[\text{Tri}(\text{PF}_6)_2]^{4+}$  ( $m/z$  969) are unique to the fully assembled complexes. The ATDs for these  $m/z$  values are shown as the middle panels in Figure 4. As expected, only one feature is observed in the ATDs for these unique peaks. The experimental cross sections of  $[\text{Rect}(\text{PF}_6)]^{3+}$  and

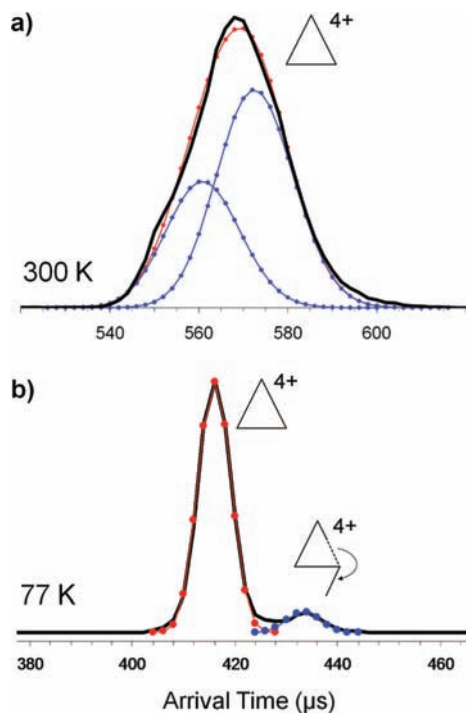
$[\text{Tri}(\text{PF}_6)_2]^{4+}$  are 361 and 580  $\text{\AA}^2$ , respectively. Their cross sections should have only a minor dependence on the charge state (see Table 1), as expected for rigid species.<sup>29,30</sup> This rigidity will be useful in determining the species present in the ambiguous peaks in the mass spectra.

One way to identify species in mass spectral peaks that could have several contributing complexes is to obtain the isotopic distribution as shown in Figure 5. Using high-resolution mass spectra, we can assign the charge,  $z$ , and hence the mass,  $m$ , in each  $m/z$  peak. For example, in Figure 5b, the isotope distribution for  $m/z$  1340 shows a spacing of 0.5 amu. To have consistency of both mass and charge, this can only be assigned to the fully assembled rectangle,  $[\text{Rect}(\text{PF}_6)_2]^{2+}$ . The  $[\text{Rect}_{1/2}(\text{PF}_6)]^+$  possibility at this  $m/z$  would have isotope peaks separated by 1.0 amu and can only be present in very minor

(29) Megyes, T.; Jude, H.; Grosz, T.; Bako, I.; Radnai, T.; Tarkanyi, G.; Palinkas, G.; Stang, P. J. *J. Am. Chem. Soc.* **2005**, *127*, 10731–10738.

(30) Tarkanyi, G.; Jude, H.; Palinkas, G.; Stang, P. J. *Org. Lett.* **2005**, *7*, 4971–4973.



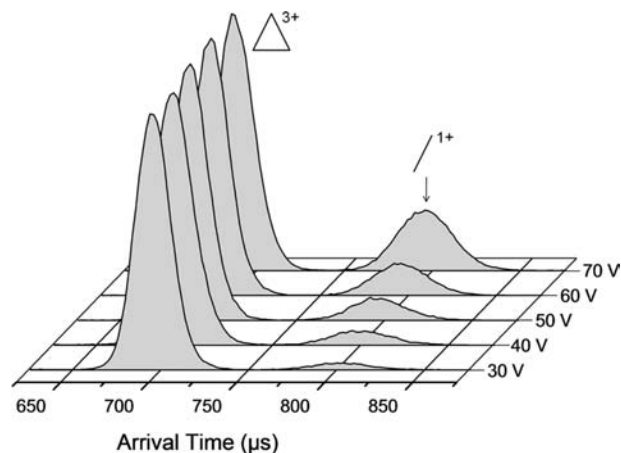


**Figure 6.** ATDs of the  $[\text{Tri}(\text{PF}_6)_2]^{4+}$  peak at  $m/z$  969 at (a) 300 and (b) 77 K. The solid line is experiment, and the connected dots represent the deconvoluted theoretical distributions.

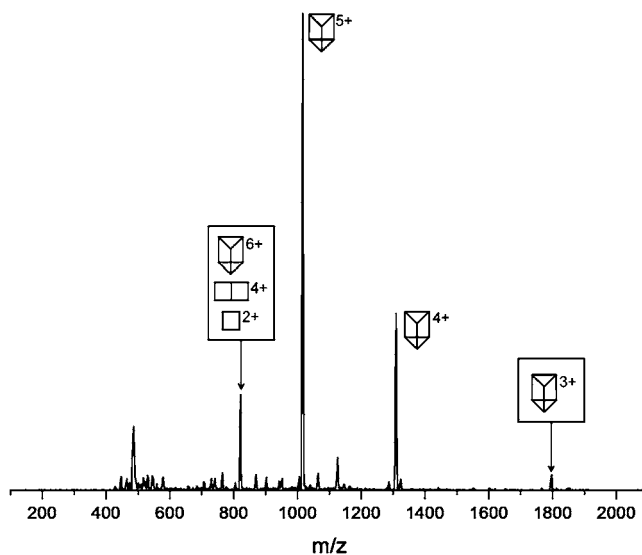
amounts or not at all. Similarly, for  $m/z$  598 in Figure 5d, the isotope spacing is also 0.5 amu, indicating this peak is due to  $\text{Rect}_{1/2}^{2+}$ . Similar analysis of isotopic data for the triangle is given in the Supporting Information.

The ATD at  $m/z$  598 in Figure 4a has only a single feature, consistent with the assignment of  $\text{Rect}_{1/2}^{2+}$  from the isotopic data in Figure 5d. The same is true for the  $\text{Tri}_{1/3}^{2+}$  peak at  $m/z$  598 in Figure 4b. However, both of the peaks at  $m/z$  1340, assigned as fully assembled  $[\text{Rect}(\text{PF}_6)_2]^{2+}$  and  $[\text{Tri}(\text{PF}_6)_3]^{3+}$  in Figure 4, have a minor additional feature present at longer times (approximately 680 and 830  $\mu\text{s}$ , respectively). In both, these minor peaks can be unambiguously assigned to monomer fragments. The arguments for these assignments are straightforward but detailed and are given in the Supporting Information.

The fully assembled  $[\text{Tri}(\text{PF}_6)_2]^{4+}$  charge state shows a single, slightly asymmetrical ATD at 300 K (Figure 4b) corresponding to an experimental cross section of  $579 \text{ \AA}^2$  and giving evidence of a shoulder indicative of multiple structures. Figure 6a shows a comparison of this ATD from Figure 4b with the asymmetry deconvoluted in the peak. Figure 6b shows the ATD of the  $[\text{Tri}(\text{PF}_6)_2]^{4+}$  charge state at 77 K. The resolving power in IMS,  $^{31,32} t/\Delta t$ , is proportional to  $(T)^{-1/2}$ . Consequently, at 77 K the resolving power is  $\sim 2$  times greater than at 300 K. As noted in Figure 6b, the 300 K ATD resolves into two peaks at 77 K. Accurate cross sections cannot be obtained at 77 K due to contributions from the ion–helium interaction potential.<sup>33</sup> However, the relative splitting is informative. Given a 300 K cross section of  $579 \text{ \AA}^2$  for the shorter time peak, the cross section for the longer time peak is approximately  $681 \text{ \AA}^2$ . The



**Figure 7.** Fragmentations of  $[\text{Tri}(\text{PF}_6)_3]^{3+}$  with increasing ion injection energy (IIE). ATDs have been normalized.

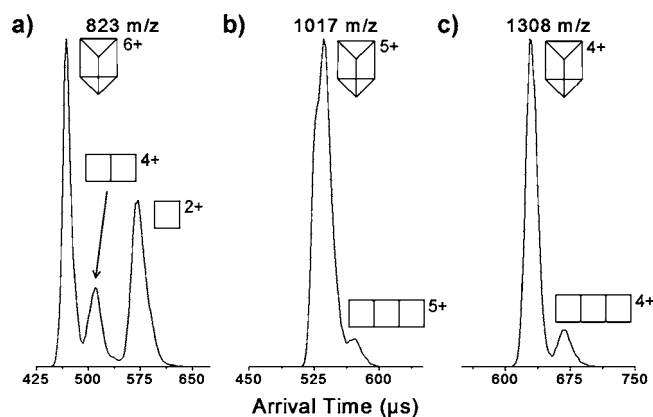


**Figure 8.** ESI–quadrupole mass spectrum of  $\text{Prism}(\text{OTf})_{12}$ . The symbols represent intact parent ions or fragments consisting of one or two “side” panels.

two peaks at 77 K can be assigned to the fully assembled triangle (shorter time major peak) and an open structure (longer time minor peak) in which a Pt–N bond breaks, allowing the side of the triangle to rotate as shown in Figure 6b. Of interest is the fact that at 300 K the intact triangle appears to be the minor feature and at 77 K it is the major component, indicating a temperature dependence in the ring-opening reaction. This possibility is being further explored and will be reported elsewhere.

Ion injection energy (IIE) can be adjusted by increasing or decreasing the voltage between the final lens of the ion funnel and the entrance to the drift cell to give the ions more or less kinetic energy as they enter the drift cell. Collisions with the helium buffer gas first increase the internal energy of the ion and then deactivate the ions back to thermal energy.<sup>34</sup> IIE studies on the fully assembled  $[\text{Tri}(\text{PF}_6)_3]^{3+}$  ion are given in Figure 7. The minor feature at longer arrival times increases with injection energy, which is consistent with fragmentation of  $[\text{Tri}(\text{PF}_6)_3]^{3+}$  as its internal energy increases. Similar studies on the assembled rectangle did not show fragmentation in this energy range (see Supporting Information). We thus conclude that the fully

- (31) Kemper, P. R.; Bowers, M. T. *J. Phys. Chem.* **1991**, *95*, 5134–5146.  
 (32) Wytttenbach, T.; Bowers, M. T. *Top. Curr. Chem.* **2003**, *225*, 207–232.  
 (33) Wytttenbach, T.; von Helden, G.; Batka, J. J., Jr.; Carlat, D.; Bowers, M. T. *J. Am. Soc. Mass. Spectrom.* **1997**, *8*, 275–282.



**Figure 9.** ATDs for various prism charge states showing fragments at the same  $m/z$ .

assembled triangle is less stable than the fully assembled rectangle under these conditions.

**Rectangle and Triangle Cross Section Calculations.** There is good agreement between experimental IMS-MS cross sections and calculated cross sections using the projection method<sup>35,36</sup> for these compounds (see Table 1) and reasonably good agreement with cross sections obtained by the trajectory method.<sup>37</sup> Systematic differences are observed using both methods, however, in part due to inadequate treatment of the ion–He interaction potential. This issue will be dealt with in detail in a separate publication.<sup>38</sup> However, it is important to note that the experimental cross sections are very well reproduced by the theoretical cross sections, giving strong support to the structural assignments made.


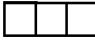
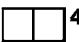
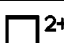

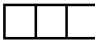


**Prism IMS-MS.** The ESI–quadrupole mass spectrum of  $\text{Prism}(\text{OTf})_{12}$  is shown in Figure 8. The peaks at  $m/z$  1308 and 1017 are unique to the fully assembled  $[\text{Prism}(\text{OTf})_7]^{4+}$  and  $[\text{Prism}(\text{OTf})_7]^{5+}$  species, respectively. The ATD for  $m/z$  823 shown in Figure 9a has three peaks which correspond to the

species  $[\text{Prism}(\text{OTf})_6]^{6+}$ ,  $[\text{Prism}_{2/3}(\text{OTf})_4]^{4+}$ , and  $[\text{Prism}_{1/3}(\text{OTf})_2]^{2+}$ . The middle peak in the ATD in Figure 9a has a cross section of either  $444 \text{ \AA}^2$  if it is  $[\text{Prism}_{2/3}(\text{OTf})_4]^{4+}$  or  $666 \text{ \AA}^2$  if it is the open form of the fully assembled prism. Model calculations (Table 2) indicate the  $666 \text{ \AA}^2$  cross section is significantly larger than expected for the open prism, but the  $444 \text{ \AA}^2$  cross section fits  $[\text{Prism}_{2/3}(\text{OTf})_4]^{4+}$  very well. Hence, the latter species is assigned to this feature in the ATD. This assignment is supported by IIE studies, which will be discussed shortly.

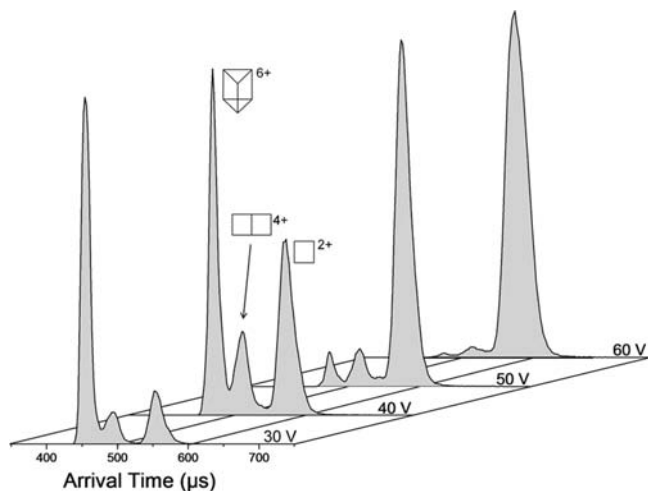
The ATDs for the  $[\text{Prism}(\text{OTf})_8]^{4+}$  and  $[\text{Prism}(\text{OTf})_7]^{5+}$  charge states (see Figure 9b,c) both show two peaks. The major, shorter time peaks in both ATDs have identical cross sections of  $564 \text{ \AA}^2$ . These compare to theoretical cross sections of  $583\text{--}586 \text{ \AA}^2$  for the intact prism calculated by the trajectory method ( $\sim 4\%$  too large) or  $538\text{--}542 \text{ \AA}^2$  by the projection calculations ( $\sim 4\%$  too small). The small peaks at longer times have experimental cross sections of  $637 \text{ \AA}^2$  that compare to trajectory cross sections of  $632$  and  $653 \text{ \AA}^2$  for fully unfolded  $[\text{Prism}(\text{OTf})_8]^{4+}$  and  $[\text{Prism}(\text{OTf})_7]^{5+}$ . These unfolded conformations appear to be the only possible structures for the small peaks at longer times in the ATDs since these charge states are unique to the  $m/z$  of the fully assembled prism and thus fragment contributions are excluded.

We again studied the fragmentation process by increasing the ion injection energy. Figure 10 shows that the relative ion population at  $m/z$  823 shifts from the unfragmented parent  $[\text{Prism}(\text{OTf})_6]^{6+}$  at low energies to the totally fragmented  $[\text{Prism}_{1/3}(\text{OTf})_2]^{2+}$  monomer at high energies while passing through the intermediate  $[\text{Prism}_{2/3}(\text{OTf})_2]^{4+}$  fragment at intermediate energies. It is also observed that significant decomposition occurs in less than 30 min upon exposure of  $\text{Prism}(\text{OTf})_{12}$  acetone solutions to air, an effect only observed after a few hours for the rectangle and triangle species. Together with the IIE study, this implies that larger species (such as the prism)

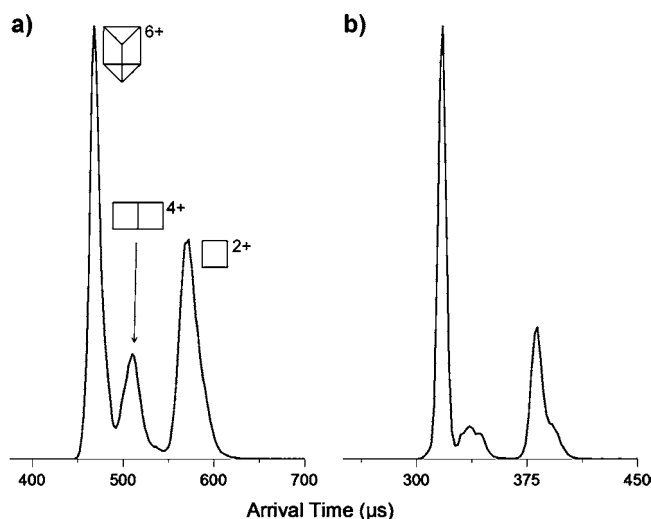
**Table 2.** Experimental and Theoretical Cross Sections for the Prism Species

Ion	$m/z$	$\sigma_{\text{expt}}$ ( $\text{\AA}^2$ )	$\sigma_{\text{calc}}^{\text{sig. } a}$ ( $\text{\AA}^2$ )	$\sigma_{\text{calc}}^{\text{trj. } a}$ ( $\text{\AA}^2$ )
$[\text{Prism}(\text{OTf})_6]^{6+}$ 	823	561	539	576
$[\text{Prism}(\text{OTf})_6]^{6+}$ 	823	n/a <sup>b</sup>	610	654
$[\text{Prism}_{2/3}(\text{OTf})_4]^{4+}$ 	823	444	454	459
$[\text{Prism}_{1/3}(\text{OTf})_2]^{2+}$ 	823	281	279	284
$[\text{Prism}(\text{OTf})_7]^{5+}$ 	1017	564	538	586
$[\text{Prism}(\text{OTf})_7]^{5+}$ 	1017	637	612	653
$[\text{Prism}(\text{OTf})_8]^{4+}$ 	1308	564	542	583
$[\text{Prism}(\text{OTf})_8]^{4+}$ 	1308	637	620	632

<sup>a</sup> sig = projection method;<sup>35,36</sup> trj = trajectory method.<sup>37</sup> <sup>b</sup> Ion is not observed experimentally.



**Figure 10.** Fragmentation of Prism(OTf)<sub>6</sub><sup>6+</sup> with increasing ion injection energy. ATDs have been normalized.

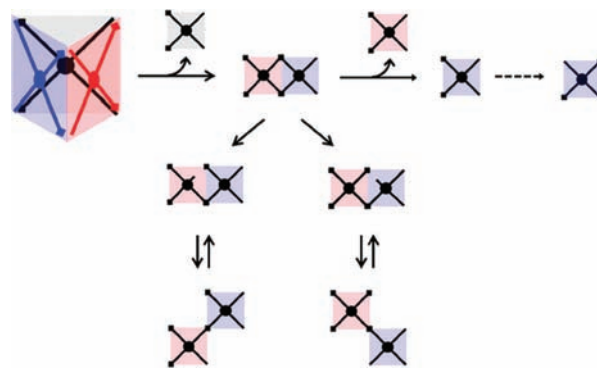


**Figure 11.** Comparison of (a) 300 and (b) 77 K Prism(OTf)<sub>6</sub><sup>6+</sup>, Prism<sub>2/3</sub>-(OTf)<sub>4</sub><sup>4+</sup>, and Prism<sub>1/3</sub>(OTf)<sub>2</sub><sup>2+</sup> structures at *m/z* 823. Broad features are resolved into at least two components for the 4+ and 2+ fragments.

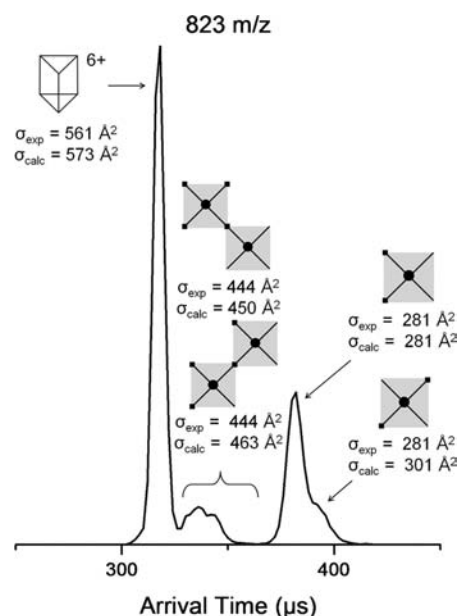
with higher charges are less stable than smaller species (such as the rectangle) with lower charges.

Molecular dynamics model calculations (see Supporting Information) for the intact prism indicate that five of the triflate anions are distributed uniformly around the outside of the prism, while three triflates fill the internal cavity. The anions enter the cavity even when different starting structures place them at various points external to the prism. Good agreement of this model structure with experiment is observed (Table 2).

A comparison of 300 and 77 K ATDs is given in Figure 11 for the *m/z* 823 species. The 77 K study that shows the ATDs



**Figure 12.** Scheme for prism fragmentation giving 4+ and 2+ species and possible isomers. For an explanation of the symbols used, see Figure 2.



**Figure 13.** Low-temperature ATD showing isomers assigned to the 4+ and 2+ charge states. The cross sections are those measured for the 300 K unresolved peaks. The separation observed at 77 K is consistent with the expected cross sections of the isomers shown.

for the 4+ and 2+ fragments have additional components. Figure 12 presents a scheme detailing the possible structures which can arise from prism monomer fragments and their isomers produced by alternative bond-breaking scenarios. These isomers are assigned to 77 K ATD peaks in Figure 13 on the basis of their relative cross sections and a comparison of experimental and theoretical cross sections for each species as shown. Stang et al.<sup>21,39</sup> made the observation that there exist both MMM and PPP optical isomers; however, these isomers have identical cross sections and cannot be resolved by ion mobility.

**Prism Calculations.** The experimental and calculated cross sections for various charge states and fragments arising from the prism structure are summarized in Table 2. In general, the projection method gives calculated cross sections which are too small by several percent, and the trajectory method cross sections are too large by a few percent. This is not unexpected, given prior experience with these two methods in this size range. The important conclusion is that the experimental cross sections are bracketed by these two calculation methods, strongly

- (34) Bernstein, S. L.; Wyttenbach, T.; Baumketner, A.; Shea, J.-E.; Bitan, G.; Teplow, D. B.; Bowers, M. T. *J. Am. Chem. Soc.* **2005**, *127*, 2075–2084.
- (35) von Helden, G.; Hsu, M. T.; Gotts, N.; Bowers, M. T. *J. Phys. Chem.* **1993**, *97*, 8182–8192.
- (36) von Helden, G.; Wyttenbach, T.; Bowers, M. T. *Int. J. Mass Spectrom. Ion Processes* **1995**, *146–147*, 349–364.
- (37) Mesleh, M. F.; Hunter, J. M.; Shvartsburg, A. A.; Schatz, G. C.; Jarrold, M. F. *J. Phys. Chem.* **1996**, *100*, 16082–16086.
- (38) Bleiholder, C.; Anderson, S. E.; Brocker, E. R.; Contreras, S. C.; Stang, P. J.; Northrop, B. H.; Bowers, M. T., manuscript in preparation.
- (39) Yuan, Q. H.; Yan, C. J.; Yan, H. J.; Wan, L. J.; Northrop, B. H.; Jude, H.; Stang, P. J. *J. Am. Chem. Soc.* **2008**, *130*, 8878–8879.



supporting the assignments made. These data also offer the opportunity to improve the parametrization of both methods.

### Conclusion

Ion mobility spectrometry–mass spectrometry has been successful in studying rigid coordination-based supramolecular structures and their mass spectra, allowing structural assignment to be made to various features observed. Excellent agreement is found for cross sections obtained from the known X-ray structures of the rectangle and triangle species with those obtained by ion mobility. This gives confidence in the assignment of the structures of the various prism species where structures have not yet been established. It also indicates that IMS-MS can be a powerful new tool in supramolecular structure determination and is complementary to existing methods such as X-ray and NMR.

The ion mobility data for these systems present an opportunity to fine-tune parameters used in the cross section calculations

by both the projection and trajectory methods. A complete study of the temperature dependence of the ion mobility cross sections is necessary to obtain such parameters and will be the subject of a future publication.<sup>38</sup>

**Acknowledgment.** The Air Force Office of Scientific Research under grant F49620-03-1-0046 (M.T.B.) is gratefully acknowledged for support of this work. P.J.S. thanks the NIH (Grant GM-57052) and B.H.N. thanks the NIH (Grant GM-080820) for support of this work. M.T.B. also gratefully acknowledges the donation of the prototype Synapt HDMS instrument by Waters Corp.

**Supporting Information Available:** Assignment of Rect(PF<sub>6</sub>)<sub>4</sub> fragments and Tri(PF<sub>6</sub>)<sub>6</sub> parent ions and fragments in mass spectra and ATDs. This material is available free of charge via the Internet at <http://pubs.acs.org>.

JA105702Y